TITLE:

Charge Exchange X-Ray Emission Detected in Multiple Shells of Supernova Remnant G296.1-0.5

AUTHOR(S):

Tanaka, Yukiko; Uchida, Hiroyuki; Tanaka, Takaaki; Amano, Yuki; Koshiba, Yosuke; Go Tsuru, Takeshi; Sano, Hidetoshi; Fukui, Yasuo

CITATION:

Tanaka, Yukiko ...[et al]. Charge Exchange X-Ray Emission Detected in Multiple Shells of Supernova Remnant G296.1-0.5. The Astrophysical Journal 2022, 933(1): 101.

ISSUE DATE:

2022-07-01

URL:

http://hdl.handle.net/2433/278456

RIGHT:

© 2022. The Author(s). Published by the American Astronomical Society.; Original content from this work may be used under the terms of the Creative Commons Attribution 4.0 licence. Any further distribution of this work must maintain attribution to the author(s) and the title of the work, journal citation and DOI.

京都大学学術情報リポジトリ
KURENAI 紅
Kyoto University Research Information Repository

京都大学 KYOTO UNIVERSITY
A Self-archived copy in
Kyoto University Research Information Repository
https://repository.kulib.kyoto-u.ac.jp
京都大学学術情報リポジトリ KURENAI 紅 Kyoto University Research Information Repository

The Astrophysical Journal, 933:101 (8pp), 2022 July 1 https://doi.org/10.3847/1538-4357/ac738f
© 2022. The Author(s). Published by the American Astronomical Society.
OPEN ACCESS

Charge Exchange X-Ray Emission Detected in Multiple Shells of Supernova Remnant G296.1–0.5

Yukiko Tanaka[1], Hiroyuki Uchida[1], Takaaki Tanaka[2], Yuki Amano[1], Yosuke Koshiba[1], Takeshi Go Tsuru[1], Hidetoshi Sano[3], and Yasuo Fukui[4]
[1] Department of Physics, Kyoto University, Kitashirakawa Oiwake-cho, Sakyo, Kyoto, Kyoto 606-8502, Japan; tanaka.yukiko.x13@kyoto-u.jp
[2] Department of Physics, Konan University, 8-9-1 Okamoto, Higashinada, Kobe, Hyogo 658-8501, Japan
[3] Faculty of Engineering, Gifu University, 1-1 Yanagido, Gifu 501-1193, Japan
[4] Department of Physics, Nagoya University, Furo-cho, Nagoya, Aichi 464-8601, Japan
Received 2022 February 7; revised 2022 May 16; accepted 2022 May 19; published 2022 July 6

Abstract

Recent high-resolution X-ray spectroscopy revealed the possible presence of charge exchange (CX) X-ray emission in supernova remnants (SNRs). Although CX is expected to take place at the outermost edges of SNR shells, no significant measurement has been reported so far due to the lack of nearby SNR samples. Here we present an X-ray study of SNR G296.1−0.5, which has a complicated multiple-shell structure, with the Reflection Grating Spectrometer on board XMM-Newton. We select two shells in different regions and find that in both regions the O VII line shows a high forbidden-to-resonance (f/r) ratio that cannot be reproduced by a simple thermal model. Our spectral analysis suggests a presence of CX and the result is also supported by our new radio observation, where we discover evidence of molecular clouds associated with these shells. Assuming G296.1−0.5 has a spherical shock, we estimate that CX is dominant in a thin layer with a thickness of 0.2%–0.3% of the shock radius. The result is consistent with a previous theoretical expectation and we therefore conclude that CX occurs in G296.1−0.5.

Unified Astronomy Thesaurus concepts: Interstellar medium (847); Supernova remnants (1667); Charge exchange recombination (2062)

1. Introduction

High-resolution X-ray spectroscopy is one of the key methods to investigate plasma conditions and radiation mechanisms of astronomical objects. Plasma diagnostics for supernova remnants (SNRs) provides us with important clues to understand interactions between expanding shocks and ambient media. In this context, previous studies were performed mainly with the Reflection Grating Spectrometer (RGS; den Herder et al. 2001) on board XMM-Newton; some of them revealed anomalously high forbidden-to-resonance intensity ratios (f/r ratios) of the O VII Heα line (e.g., van der Heyden et al. 2003; Broersen et al. 2011). Although their physical origin is still unclear, recent studies indicate that charge exchange (CX) is one of the possibilities to explain the high f/r ratio (e.g., Katsuda et al. 2012; Uchida et al. 2019; Koshiba et al. 2022).

CX takes place when highly charged ions collide with a cold neutral matter population. Thus, indicating that SNR-cloud interaction regions are plausible candidates to detect CX X-ray emission. Since the CX cross section for ions of light elements (e.g., O^{8+}) peaks at a few thousand km s^{-1} (e.g., Gu et al. 2016), evolved SNRs are the best targets to search for CX X-ray emissions. Possible detections are indeed reported from observations of middle-aged SNRs such as Puppis A (Katsuda et al. 2012) and the Cygnus Loop (Uchida et al. 2019). If CX is occurring in these SNRs, its emitting region would be the outer edge of the shock front (a few percent of the shock radius) in contact with dense clouds (Lallement 2004). However, a quantitative measurement together with direct evidence for cloud interactions are both missing so far in previous studies.

G296.1−0.5 is a nearby middle-aged (∼20,000 yr; Hwang & Markert 1994) SNR with a diameter of 35–50 pc (assuming a distance of 4 kpc; Longmore et al. 1977). Previous radio and X-ray observations revealed a complex asymmetric morphology, especially a double-shell structure in the south (Markert et al. 1981; Whiteoak & Green 1996), which implies a dense inhomogeneous medium in the vicinity of the remnant. This is supported by Castro et al. (2011), who performed X-ray imaging and spectral analysis of G296.1−0.5 with XMM-Newton and concluded that this remnant is of Type Ib/c origin evolved in a dense environment. The presence of the dense ambient medium is suggested also by Hα emissions detected at several locations over G296.1−0.5 (Gaustad et al. 2001). These characteristics are common with Puppis A and the Cygnus Loop, and thus G296.1−0.5 can be another potential candidate for a CX-dominant SNR.

In this paper, we perform a high-resolution spectroscopy for two shells of G296.1−0.5 using the RGS, mainly focusing on detection of the CX X-ray emissions. We also carry out a ^{12}CO(J = 1–0) and H I observation to probe molecular clouds and atomic gas around the remnant. These observations enable us to investigate physical conditions that enhance the contribution of CX in SNRs. Throughout the paper, errors are given at the 68% confidence level.

2. Observations and Data Reduction

G296.1−0.5 was observed four times with XMM-Newton from 2007 to 2010. Each observation targets different parts of the SNR so as to cover the whole remnant. Among them, one of the observations of the southwestern region was

Original content from this work may be used under the terms of the Creative Commons Attribution 4.0 licence. Any further distribution of this work must maintain attribution to the author(s) and the title of the work, journal citation and DOI.

京都大学 KYOTO UNIVERSITY
A Self-archived copy in
Kyoto University Research Information Repository
https://repository.kulib.kyoto-u.ac.jp
京都大学学術情報リポジトリ KURENAI 紅 Kyoto University Research Information Repository

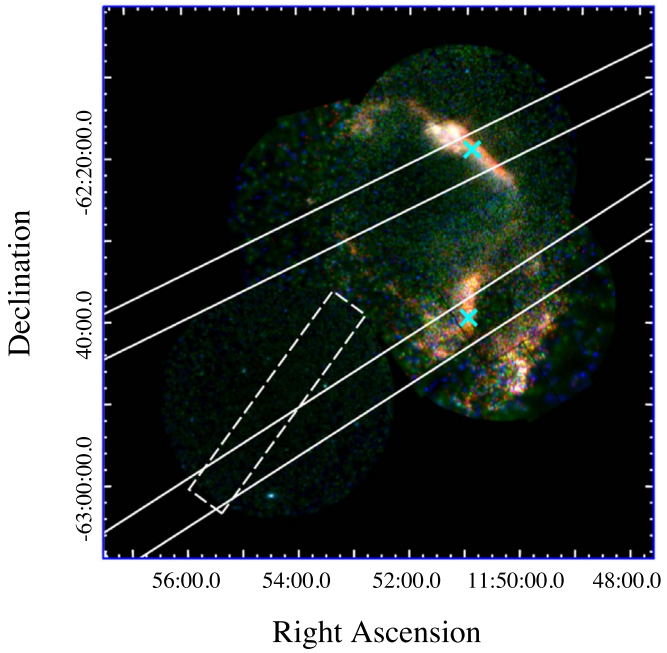

Figure 1. Three-color image of G296.1−0.5. Red, green, and blue correspond to the 0.3–0.7 keV, 0.7–1.0 keV, and 1.0–1.5 keV energy bands. The white lines represents the cross-dispersion widths of the RGS (5′). The white dotted rectangle shows the region used as a background. The cyan X marks are the center of each source position; $(\alpha_{2000}, \delta_{2000}) = (11^{h}50^{m}54\overset{s}{.}5059, -62°19'03\overset{''}{.}44)$, $(11^{h}50^{m}57\overset{s}{.}2627, -62°38'46\overset{''}{.}40)$ for NW and SE, respectively.

contaminated by a stellar flare that occurred in the field of view (FOV). We therefore used only another data set (Obs. ID 0503220201) for the southeast. Those of the northwestern (Obs.ID 0503220101) and eastern (Obs.ID 0503220301) shell regions were also used for the following imaging analysis. To perform a high-resolution spectroscopy, we selected two data sets (northwest and southeast; hereafter, NW and SE), in which the shells are along the cross-dispersion direction in the RGS FOV, since the energy resolution of the RGS highly depends on the source width. A nearby blank-sky observation (Obs. ID 0804240201) outside the SNR was used to estimate the background.

We used XMM Science Analysis Software version 18.0.0 for the following analysis. The European Photon Imaging Camera Metal Oxide Semi-conductor (EPIC MOS; Turner et al. 2001) data were processed using the XMM-Newton Extended Source Analysis Software package with background processing based on the modeling of Snowden et al. (2004). Figure 1 shows a vignetting-corrected three-color image of G296.1−0.5. We set the brightest locations of the NW and SE shells as the "source positions" (Figure 1) and processed the RGS data using the standard pipeline tool `rgsproc`. The good time interval was determined based on the count rate of CCD9, which is closest to the optical axis of the telescope and most affected by background flares.

As a result of the above procedure, we obtained effective times for each instrument as summarized in Table 1. Note that we used only first-order spectra since second-order spectra do not have sufficient statistics. Model fitting was performed in the range of 8.3–31 Å (0.40–1.5 keV) since backgrounds dominate outside the range.

Table 1
Observation Data

Region	Observation ID	Starting Time	Effective Exposure Time (ks)	
			MOS	RGS
NW	0503220101	2007 Jul 7	22.2	25.4
SE	0503220201	2007 Jul 15	4.4	25.8
East	0503220301	2007 Dec 24	7.7	⋯
Background	0804240201	2018 Feb 8	94.0	117.3

Note. The effective time of MOS represents the sum of MOS 1 and MOS 2. The same is true for RGS.

3. Spectral Analysis

The RGS spectra extracted from the NW and SE shells are displayed in Figure 2. Clearly visible in the spectra are the Mg XI Heα (9.2 Å), Ne IX Heα (13.5 Å), Fe XVII (15.0 Å; 17.0 Å), O VIII Lyα (19.0 Å), O VII Heα (∼22 Å), N VII Lyα (24.8 Å), and N VI Heα (28.8 Å) lines. We found that the O VII Heα line is clearly resolved into the resonance and forbidden lines and that the forbidden line seems relatively stronger than the resonance line especially in the spectrum of the SE. The following spectral fitting was performed simultaneously for the RGS1/2 and MOS1/2 spectra. We used SPEX version 3.06.01 (Kaastra et al. 1996) for the spectral fit with the maximum likelihood W-statistic (Wachter et al. 1979). To take into account the spatial extent of the source, we multiplied a spectral model with `Lpro`,[5] which convolves a model function with a surface brightness profile, including a point-spread function, which is estimated from the MOS1 image (Tamura et al. 2004).

We first tried fitting the spectra with the nonequilibrium ionization (NEI) model `neij` absorbed by neutral gas with cosmic abundances (Morrison & McCammon 1983). This "NEI×abs" model was used also in the analysis by Castro et al. (2011) of the EPIC MOS data. We set the volume emission measure $\mathrm{VEM_{NEI}}$ ($= n_e n_p V_{\mathrm{NEI}}$, where n_e, n_p, and V_{NEI} are the electron density, proton density, and the volume of NEI plasma, respectively), the electron temperature kT_e, and the ionization timescale $n_e t$ as variables. The abundances of N, O (=C), Ne, Mg, Fe (=Ni) were left free and the others were fixed at the solar values estimated by Lodders et al. (2009). The absorption column density N_H was also a variable.

The best-fit NEI×abs models for the NW and SE shells are shown in Figure 3. The best-fit parameters are listed in Table 2. There are large residuals at the wavelength of O VII Heα; the forbidden lines in the NW and SE spectra are significantly stronger than the prediction by the model. While the result for the NW was already implied by the result of Castro et al. (2011; see their Figure 5), we discovered that the SE shell also shows a similar sign of a strong forbidden line.

For more quantitative discussion on the f/r ratios, we calculated the ratios by replacing the O VII lines in the best-fit model with Gaussians, and obtained $0.81^{+0.21}_{-0.15}$ and $2.1^{+0.9}_{-0.5}$ for the NW and SE shells, respectively (see Table 3). Figure 4 shows f/r ratios expected from the NEI model as a function of kT_e in the range of possible ionization states $n_e t$. We found that the observed f/r ratio for the NW requires an extremely low temperature (<0.2 keV) if we assume a simple NEI model. The result is inconsistent with the best-fit value of

[5] https://spex-xray.github.io/spex-help/models/lpro.html

京都大学 KYOTO UNIVERSITY
A Self-archived copy in
Kyoto University Research Information Repository
https://repository.kulib.kyoto-u.ac.jp
京都大学学術情報リポジトリ KURENAI 紅 Kyoto University Research Information Repository

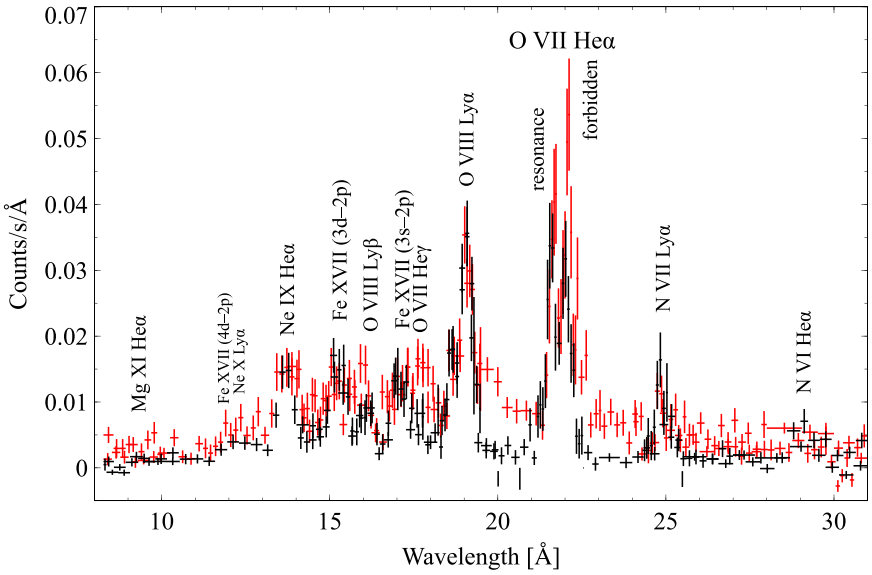

Figure 2. RGS spectra of the NW shell (black) and the SE shell (red).

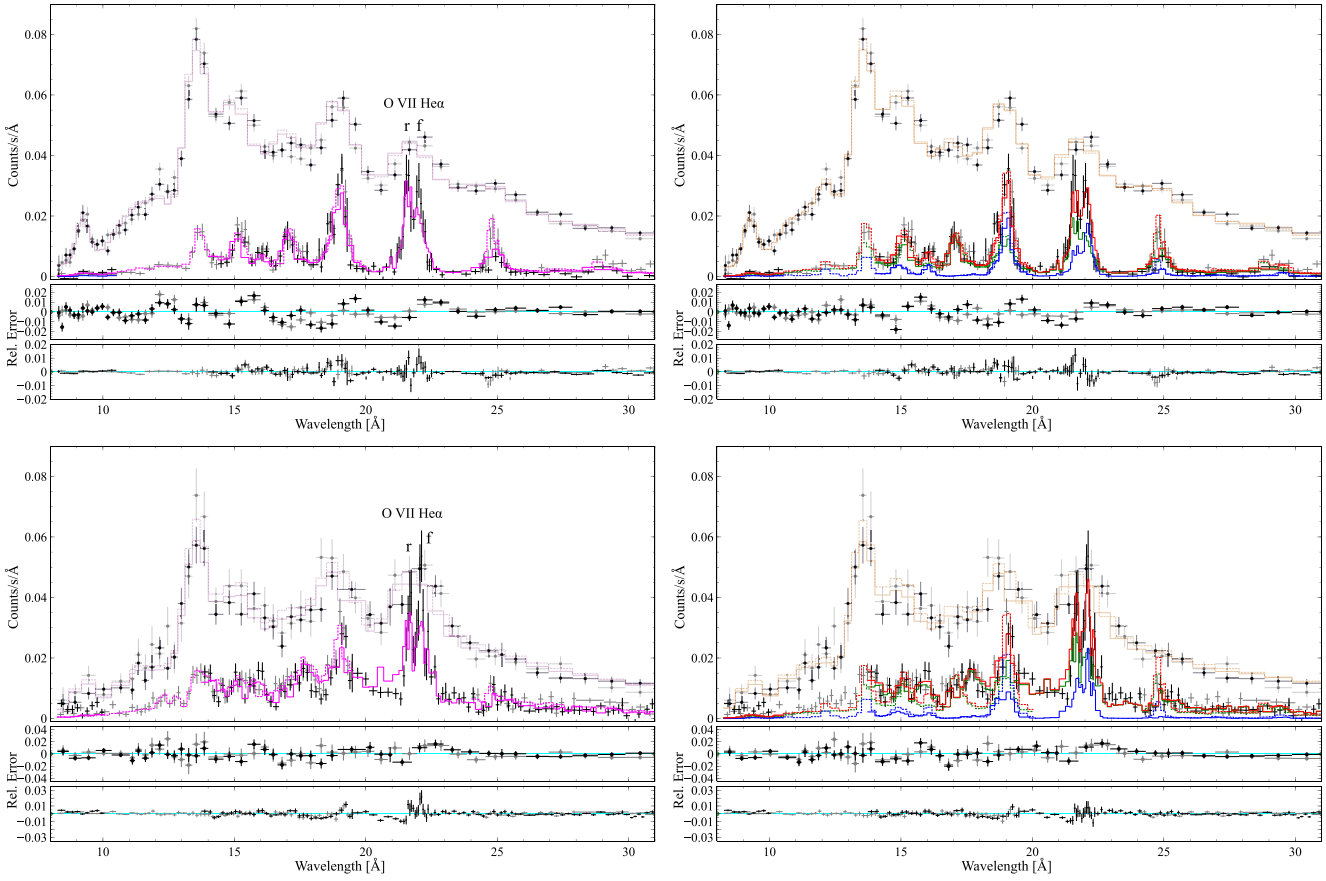

Figure 3. Top: MOS1 (black circle), MOS2 (gray circle), RGS1 (black cross), and RGS2 (gray cross) spectra of the NW shell. The solid and dotted lines are the best-fit models for MOS1/RGS1 and MOS2/RGS2, respectively. The MOS spectra are scaled by a factor of 0.5 for a displaying purpose. The best-fit results of the NEI×abs and (NEI+CX)×abs models are shown in the left and right panels, respectively. The middle and lower panels in each figure represent the residuals for the MOS and the RGS, respectively. Bottom: same as the top panels, but for the SE shell.

$kT_e = 0.48$–0.56 keV and, furthermore, such a low-temperature plasma cannot emit detectable O VII lines due to insufficient amounts of O^{6+} ions; the same is true also for the SE shell. Therefore, another physical process is needed to explain the high f/r ratios in G296.1−0.5.

Resonance scattering (RS) is one of the possibilities that can enhance the f/r ratio. RS is considered to be effective for an SNR with an asymmetric morphology and optically thick plasma depth along the line of sight (Kaastra & Mewe 1995). Clear observational evidence for RS was first discovered by

京都大学 KYOTO UNIVERSITY
A Self-archived copy in
Kyoto University Research Information Repository
https://repository.kulib.kyoto-u.ac.jp
京都大学学術情報リポジトリ KURENAI 紅 Kyoto University Research Information Repository

Table 2
Best-fit Parameters

Region	Parameter	NEI × abs	(NEI + CX) × abs
NW	$N_{\rm H}$ (10^{20}cm^{-2})	$\leqslant 2.4$	$5.3^{+1.8}_{-1.1}$
	$kT_{\rm e}$ (keV)	$0.50^{+0.06}_{-0.02}$	$0.40^{+0.01}_{-0.01}$
	$n_{\rm e}t$ (10^{10}s cm^{-3})	$2.8^{+0.3}_{-0.4}$	$3.0^{+0.3}_{-0.3}$
	$v_{\rm col}$ (km s^{-1})	...	394^{+72}_{-48}
	N	$0.87^{+0.20}_{-0.11}$	$0.63^{+0.07}_{-0.07}$
	O(=C)	$0.33^{+0.06}_{-0.03}$	$0.17^{+0.02}_{-0.02}$
	Ne	$0.54^{+0.12}_{-0.04}$	$0.36^{+0.03}_{-0.04}$
	Mg	$0.41^{+0.10}_{-0.04}$	$0.38^{+0.05}_{-0.05}$
	Fe(=Ni)	$0.39^{+0.09}_{-0.04}$	$0.33^{+0.03}_{-0.03}$
	$\rm VEM_{NEI}$(10^{56}cm^{-3})	$0.6^{+0.1}_{-0.2}$	$1.0^{+0.3}_{-0.1}$
	$\rm VEM_{CX}$(10^{56}cm^{-3})	...	$1.1^{+0.9}_{-0.2}$
	W-statistic/dof	4382/3905	4247/3902
SE	$N_{\rm H}$ (10^{20}cm^{-2})	$18.9^{+6.9}_{-1.3}$	$\leqslant 7.3$
	$kT_{\rm e}$ (keV)	$0.204^{+0.008}_{-0.047}$	$0.37^{+0.06}_{-0.02}$
	$n_{\rm e}t$ (10^{10}s cm^{-3})	$17\leqslant$	$3.8^{+0.8}_{-1.0}$
	$v_{\rm col}$ (km s^{-1})	...	$\leqslant 213$
	N	$0.12^{+0.04}_{-0.05}$	$0.32^{+0.14}_{-0.5}$
	O(=C)	$0.17^{+0.02}_{-0.03}$	$0.20^{+0.05}_{-0.02}$
	Ne	$0.24^{+0.05}_{-0.05}$	$0.31^{+0.09}_{-0.03}$
	Mg	$0.35^{+0.10}_{-0.09}$	$0.28^{+0.11}_{-0.07}$
	Fe(=Ni)	$0.09^{+0.02}_{-0.02}$	$0.20^{+0.10}_{-0.02}$
	$\rm VEM_{NEI}$(10^{56}cm^{-3})	35^{+65}_{-7}	$2.2^{+0.5}_{-1.0}$
	$\rm VEM_{CX}$(10^{56}cm^{-3})	...	$1.7^{+0.7}_{-1.0}$
	W-statistic/dof	4448/3872	4398/3869

Note. The abundances are calculated relative to the proto-Solar abundances of Lodders et al. (2009).

Table 3
f/r Ratios Calculated from Each Model and Data

Region	Model	Component	f/r ratio
NW	NEI × abs	NEI	0.34
	(NEI + CX) × abs	NEI	0.40
		CX	2.2
	Data		$0.81^{+0.21}_{-0.15}$
SE	NEI × abs	NEI	0.64
	(NEI + CX) × abs	NEI	0.43
		CX	3.1
	Data		$2.1^{+0.9}_{-0.5}$

Amano et al. (2020), who analyzed RGS spectra of the extra-Galactic SNR N49. Following their method to evaluate a contribution of the RS effect, we tried the "(NEI−Gaus)×abs" model, in which negative Gaussians were added to the NEI model. The four Gaussians we added represent the scattered photon fluxes of the resonance lines of O VII Heα (21.6 Å) and Ne IX Heα (13.4 Å), Fe XVII (3d–2p) (15.0 Å), and O VIII Lyα (19.0 Å), which have high oscillator strengths. From the best-fit results, the values of W-statistic/d.o.f. are 4256/3901 and 4411/3868 for the NW and SE, respectively. While a possibility of RS cannot be ruled out from a statistical point of view, we found that the model does not significantly improve the residuals around the O VII Heα line as presented in Figure 5. We therefore conclude that RS is not the main cause for the observed anomalous f/r ratio in G296.1−0.5.

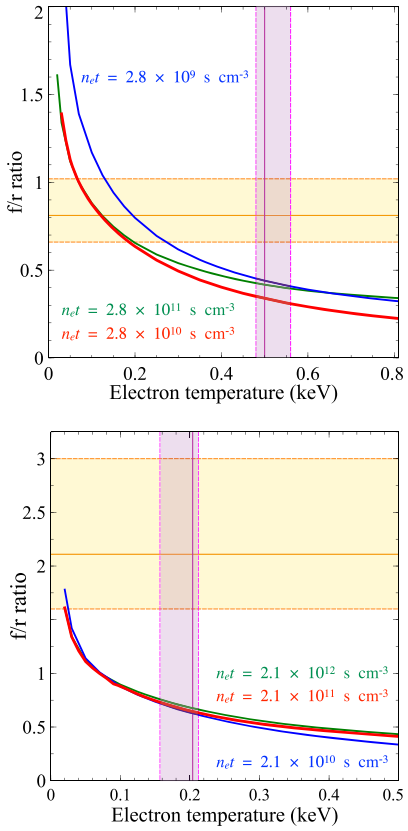

Figure 4. f/r ratio expected from an NEI model as a function of $kT_{\rm e}$. The top and bottom panels are for the NW and SE shells, respectively. The colors of each line indicate n_et assumed: The red line corresponds to the best-fit value. The orange and magenta hatched areas indicate the obtained f/r ratio and the best-fit kT_e, respectively.

CX is another possibility to account for the high f/r ratio because the forbidden line intensity becomes relatively dominant by this process. We added the CX model (Gu et al. 2016) to the above model, "(NEI+CX)×abs", coupling all the abundances and plasma temperature with those of the NEI component. We varied the volume emission measure $\rm VEM_{CX}$ ($=n_{\rm p}n_{\rm NH}V_{\rm CX}$, where $n_{\rm NH}$ and $V_{\rm CX}$ are the neutral hydrogen density and the effective interaction volume, respectively) and the collision velocity $v_{\rm col}$. We tried two collision cases, which are available in the CX model: A simpler case, which assumes a single collision for each ion, results in a physically unacceptable fit, in which $v_{\rm col}$ is much higher than that expected from a middle-aged SNR and $kT_{\rm e}$ is too low to emit X-rays. The other case assumes that one ion repeatedly captures electrons until it becomes neutral. It seems a more realistic assumption if SNR shocks are propagating into dense clouds. We applied this "multiple collision" model and confirmed that the spectra are well explained with physically reasonable parameters. The best-fit models are shown in Figure 3. The parameters are summarized in Table 2. The continuum is well reproduced by the NEI component, while the CX emission enhances the lines, in particular the O VII forbidden line, as indicated in Figure 5.

京都大学 KYOTO UNIVERSITY
A Self-archived copy in
Kyoto University Research Information Repository
https://repository.kulib.kyoto-u.ac.jp
京都大学学術情報リポジトリ KURENAI 紅 Kyoto University Research Information Repository

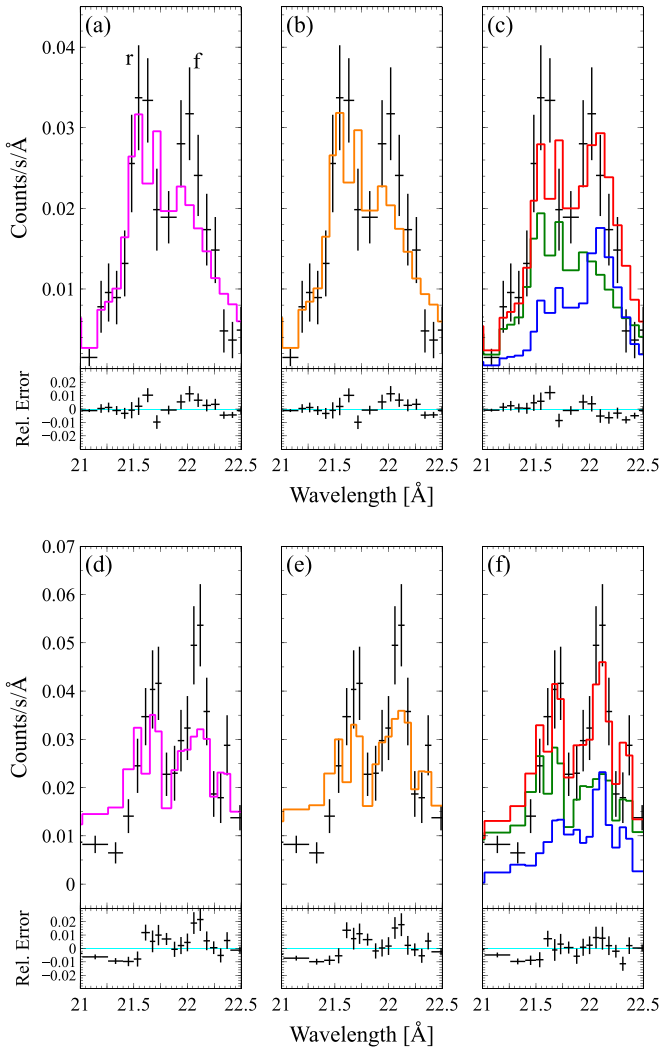

Figure 5. Close-up view of the best-fit results around the O VII line for the NW ((a)–(c)) and SE ((d)–(f)) shells. The magenta, orange, and red lines denote the NEI×abs, (NEI−Gaus)×abs, and (NEI+CX)×abs models, respectively. The NEI and CX components are shown as the green and blue lines, respectively. The bottom panels show residuals from the models.

4. Discussion

4.1. Interaction with Molecular Clouds

Through the analysis described in Section 3, we found evidence of CX in both the NW and SE shells. The detection of CX implies that the shock-heated plasma is interacting with a cold neutral gas population. The estimated collision velocities $v_{\rm col}$ are 400 km s^{-1} and 200 km s^{-1} for the NW and SE shells, respectively (Table 2). On the other hand, the shock velocity of G296.1−0.5 is $v_{\rm sh} \sim 600$ km s^{-1}, which is derived from the best-fit value of $kT_{\rm e}$, using the Rankine–Hugoniot relation under a thermal equilibrium condition $v_{\rm sh}^2 = 16kT_{\rm e}/3\mu m_{\rm H}$, where μ is the mean molecular weight (=0.6) and $m_{\rm H}$ is the hydrogen mass. Given that a plasma velocity v behind the shock equals to $3/4v_{\rm sh} \sim 450$ km s^{-1}, we found a potential discrepancy between the estimated collision velocities and the plasma velocity: $v > v_{\rm col}$. A similar result was obtained by Uchida et al. (2019) for an outermost rim of the Cygnus Loop ($v_{\rm sh} \sim 300$ km s^{-1}; $v_{\rm col} < 50$ km s^{-1}). Both results imply that ions with a bulk velocity behind the shock are slowing down and undergo collisions with a dense ambient medium, which may hint at the presence of CX in these SNRs.

To investigate the distribution of neutral molecular and atomic gas around G296.1−0.5, we analyzed ^{12}CO(J = 1–0) and H I data obtained with the NANTEN 4 m millimeter/submillimeter radio telescope (Mizuno & Fukui 2004) and the Australia Telescope Compact Array (ATCA) and Parkes 64 m radio telescope (McClure-Griffiths et al. 2005), respectively.

Figure 6 shows the velocity channel distributions of CO and H I limited to the velocity range in which the CO and H I clouds show good spatial correlation with the X-ray shell. We found three molecular clouds in the NW and SE shells (hereafter Cloud 1 and Cloud 2, respectively) and toward the southwestern rim (hereafter, Cloud 3), which are likely associated with G296.1−0.5. The distribution of H I gas at $V_{\rm LSR} = -24$ km s^{-1} to $V_{\rm LSR} = -21$ km s^{-1} is also well correlated with the X-ray shell in the west. These results imply a presence of dense gas toward the west and are also consistent with the faint X-ray emission in the east.

Figures 7(a) and (d) show the velocity integrated intensity maps of CO and H I at $V_{\rm LSR} = -30$ km s^{-1} to $V_{\rm LSR} = -15$ km s^{-1}, respectively. The spatial relation between the X-ray shell and the neutral gas is clearly revealed in each map. Figures 7(b), (c), (e), and (f) show the position–velocity (p–v) diagrams of CO and H I, respectively. We found a cavity-like distribution along with CO and H I clouds for each p–v diagram. The distribution and the spatial shift of H I suggest that the CO and H I clouds are expanding with a velocity of $\sim$10 km s^{-1} and a systemic velocity of -20 ± 4 km s^{-1}. Since the spatial extent of the CO/H I emissions is roughly consistent with the apparent diameter of the X-ray shell, we conclude that the cavity was formed by shock waves and/or a stellar wind from the progenitor of G296.1−0.5 (see Koo et al. 1990). These results confirm that Clouds 1–3 and H I gas at $V_{\rm LSR} = -30$ km s^{-1} to $V_{\rm LSR} = -15$ km s^{-1} are associated with G296.1−0.5, while further follow-up observations would be needed to obtain more detailed information such as the intensity ratio of CO J = 3–2/1–0, their line broadening, and a subparsec-scale spatial resolution (e.g., Seta et al. 1998; Sano & Fukui 2021). By adopting the standard Galactic rotation curve model with the IAU recommended values of $R_0 = 8.5$ kpc and $\Theta_0 = 220$ km s^{-1} (Kerr & Lynden-Bell 1986; Brand & Blitz 1993), we estimate the distance to the SNR to be $\sim 2.1^{+0.9}_{-0.6}$ kpc, which is consistent with a previous analysis (2–5 kpc; Castro et al. 2011) and gives a more reliable result.

From the radio observations, we speculate that the H I gas is globally associated with G296.1−0.5 in the west and contributes to the CX emission, whereas the dense clouds such as Clouds 1 and 2 are likely outside the shells. We calculate the hydrogen number density of H I gas near the clouds as $\sim$200 cm^{-3} for the NW and 160 cm^{-3} for the SE by assuming an optically thin emission (e.g., Dickey & Lockman 1990) and the depth of the H I gas to be $\sim$5 pc. Basic physical properties for each molecular cloud are listed in Table 4, for which we adopted the SNR distance of 2.1 kpc and a CO-to-H$_2$ conversion factor of 2.0 × 10^{20} cm^{-2}(K km s^{-1})$^{-1}$ (e.g., Bolatto et al. 2013).

Since a nonnegligible fraction of hydrogen atoms in molecular clouds undergo collisional ionization, a number of hydrogen atoms that can cause CX is limited. Relative probability of the CX and electron collisional ionization depends on the collision velocity and plasma temperature

京都大学 KYOTO UNIVERSITY
A Self-archived copy in
Kyoto University Research Information Repository
https://repository.kulib.kyoto-u.ac.jp
京都大学学術情報リポジトリ KURENAI 紅 Kyoto University Research Information Repository

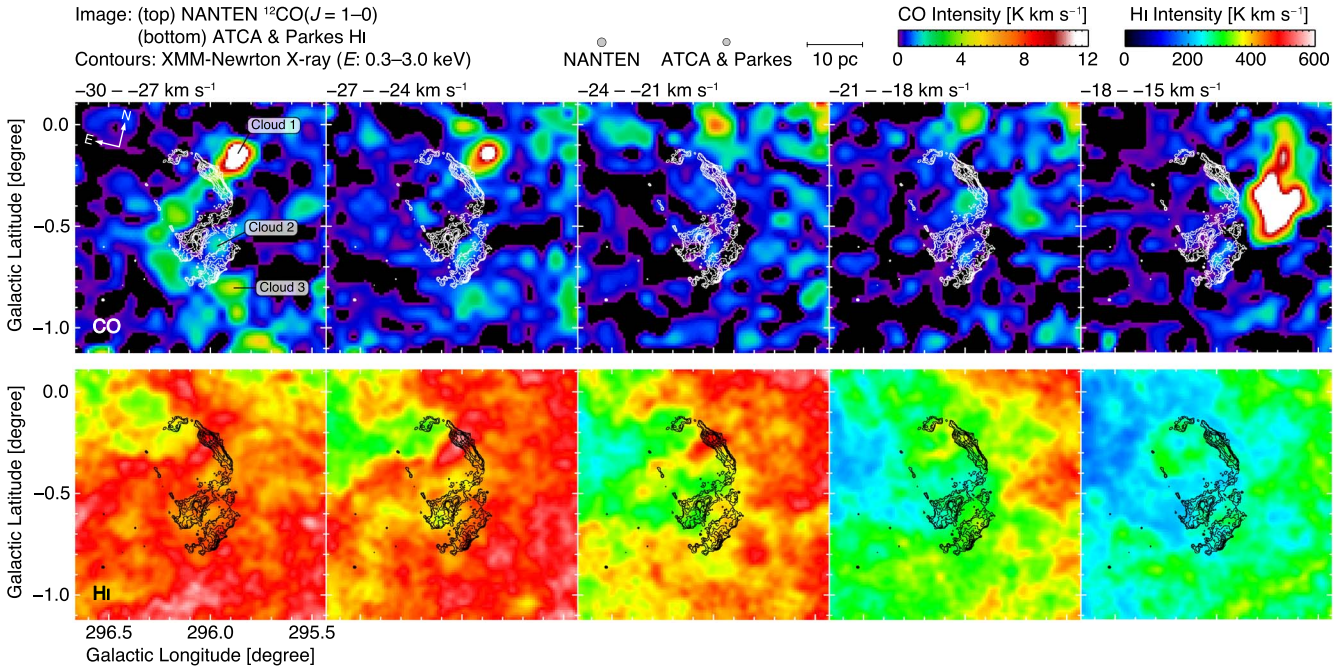

Figure 6. Velocity channel distributions of the NANTEN ^{12}CO(J = 1–0) intensities (top panels) and ATCA & Parkes H I intensities (bottom panels), superposed on the XMM-Newton X-ray intensity contours in the energy band of 0.3–3.0 keV. Each panel shows CO and H I intensity distributions integrated every 3 km s^{-1} in a velocity range from −30 to −15 km s^{-1}. The contour levels are 70, 100, 190, 340, 550, and 820 counts s^{-1} degree^{-2}. The molecular clouds 1–3 discussed in Section 4.1 are also indicated.

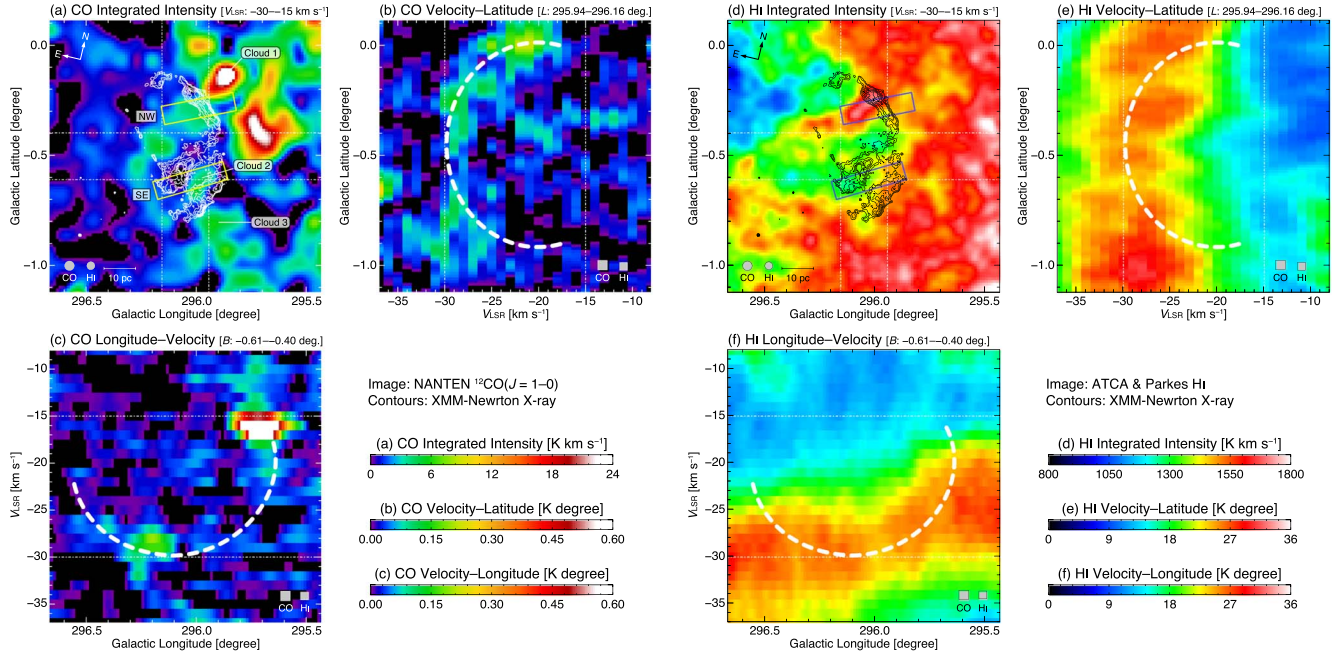

Figure 7. Velocity integrated intensity maps and position–velocity (p–v) diagrams of CO (left panels) and H I (right panels). The integration range is from −30 to −15 km s^{-1} in velocity for each intensity map ((a) and (d)); from 295.°94 to 296.°15 in Galactic longitude for each velocity–latitude diagram ((b) and (e)); and from − 0.°61 to − 0.°40 in Galactic latitude for each longitude–velocity diagram ((c) and (f)). The superposed contours are the same as shown in Figure 6. The rectangles, the NW and SE, indicate the regions used for extracting RGS spectra. Clouds 1–3 discussed in Section 4.1 are also indicated. The dashed curve in each p–v diagram represents the boundaries of the CO and H I cavities.

(Lallement 2004). If the collision velocity is high (∼1000 km s^{-1}), hot ions can stream deeply into a molecular cloud, resulting in a relatively high probability of the CX. In a case of a high temperature plasma (∼1 keV), collisional excitation is dominant and neutral hydrogen atoms are mostly ionized. Applying $v_{\rm col}$ and $kT_{\rm e}$ of the best-fit (NEI+CX)×abs models (Table 2) to the discussion by Lallement (2004; see their Figure 1), we assume that ∼30% (for the NW) and ∼20% (for the SE) of the neutral gas densities contribute to the CX process before the collisional ionization. As a result, we obtain neutral hydrogen densities $n_{\rm NH}$ to be ∼60 cm^{-3} and ∼32 cm^{-3} for the NW and SE, respectively.

京都大学 KYOTO UNIVERSITY
A Self-archived copy in
Kyoto University Research Information Repository
https://repository.kulib.kyoto-u.ac.jp
京都大学学術情報リポジトリ KURENAI 紅 Kyoto University Research Information Repository

Table 4
Physical Properties of Molecular Clouds Likely Associated with G296.1−0.5

Cloud name	α_{J2000} (^{h} ^{m} ^{s})	δ_{J2000} ($^\circ$ $'$ $''$)	T_{mb} (K)	V_{LSR} (km s^{-1})	ΔV (km s^{-1})	Size (pc)	Mass ($M_\odot$)	$n_H(H_2)$ (cm^{-3})
(1)	(2)	(3)	(4)	(5)	(6)	(7)	(8)	(9)
Cloud 1	11 50 21.15	−62 10 00.6	7.35 ± 0.14	−27.54 ± 0.04	4.28 ± 0.09	3.8	1200	1600
Cloud 2	11 50 07.41	−62 38 56.7	0.56 ± 0.13	−27.28 ± 0.55	4.84 ± 1.37	5.0	230	140
Cloud 3	11 49 05.94	−62 48 48.4	1.61 ± 0.14	−29.54 ± 0.17	4.12 ± 0.41	5.8	590	230

Note. Column (1): Cloud name. Columns (2)–(9): observed properties of clouds obtained by a single Gaussian fitting with ^{12}CO(J = 1–0) line emission. Columns (2)–(3): position of clouds in the equatorial coordinate. Column(4): peak radiation temperature. Column (5): central velocities of CO spectra. Column (6): FWHM linewidths of CO spectra ΔV. Column (7): diameters of clouds defined as $(A/\pi)^{0.5} \times 2$, where A is the surface area of each cloud surrounded by a contour of the half level of the maximum integrated intensity. Column (8): masses of clouds derived by an equation of $N(H_2)/W(CO) = 2.0 \times 10^{20}$ (K km s^{-1})$^{-1}$ cm^{-2}, where $N(H_2)$ is the molecular hydrogen column density and W(CO) is the integrated intensity of ^{12}CO(J = 1–0) (Bolatto et al. 2013). Column (9): hydrogen number densities of clouds $n_H(H_2)$. The errors of mass and $n_H(H_2)$ are ∼30% by assuming the same error in the CO-to-H_2 conversion factor (see Bolatto et al. 2013).

4.2. Emitting Region of CX

Previous theoretical calculations predict that CX occurs in a thin layer at the outermost edge of an SNR blast wave (e.g., Lallement 2004). According to an estimation for a spherical SNR, CX dominates over thermal emission in the outer layer with a "collision parameter" of $p \sim 0.99$ (Lallement 2004); when the CX-emitting region has a thickness of Δr from the shock front, p is expressed as

$$p = \frac{r_{s(\mathrm{out})} - \Delta r}{r_{s(\mathrm{out})}}, \quad (1)$$

where the outer radius of swept-up interstellar matter is $r_{s(\mathrm{out})}$. In the case of $p = 0.99$, the outer layer with a thickness of 1% of the shock radius is CX dominant. Following this result, Katsuda et al. (2011) claimed that the expected CX emission measure in the Cygnus Loop is consistent with the theoretical value. However, there was a discrepancy by a factor of 2–6. A more accurate value of p is required but a detailed measurement has not been obtained so far.

We can estimate p for the NW and SE shells since we obtained n_{NH} of the interacting molecular clouds in the CX-emitting regions. As illustrated in Figure 8, we assume a part of a spherical shell between the outer ($r_{s(\mathrm{out})}$) and inner ($r_{s(\mathrm{in})}$) radii. The ratio of the emitting volume of the CX (V_{CX}) to NEI (V_{NEI}) is described with a collision parameter p as follows:

$$\frac{V_{CX}}{V_{NEI}} = \frac{r_{s(\mathrm{out})}^3 - (r_{s(\mathrm{out})} - \Delta r)^3}{r_{s(\mathrm{out})}^3 - r_{s(\mathrm{in})}^3} = \frac{1 - p^3}{1 - \left(\frac{r_{s(\mathrm{in})}}{r_{s(\mathrm{out})}}\right)^3}. \quad (2)$$

The ratio of the volume emission measure of the CX component to that of the NEI component is

$$\frac{\mathrm{VEM_{CX}}}{\mathrm{VEM_{NEI}}} = \frac{n_p n_{NH} V_{CX}}{n_e n_p V_{NEI}} \simeq \frac{n_{NH} V_{CX}}{1.2 n_p V_{NEI}}, \quad (3)$$

where we assume the solar metallicity, i.e., $n_e \simeq 1.2 n_p$.

We get $V_{NEI} \sim 5 \times 10^{56}$ cm^3, assuming from the X-ray morphology that the NW rim is a part of a spherical shell with a thickness of 1 pc and a radius of 7 pc: $r_{s(\mathrm{out})} = 7$ pc and $r_{s(\mathrm{in})} = 6$ pc. Since the best-fit value of $\mathrm{VEM_{NEI}}$ is $1.0^{+0.3}_{-0.1} \times 10^{56}$ cm^{-3} ($=1.2 n_p^2 V_{NEI}$), we derive $n_p = 0.4$ cm^{-3} for the NW. Substituting these values into Equation (3), we obtain $V_{CX}/V_{NEI} = 9.0 \times 10^{-3}$. From Equation (2), the collision parameter in the NW shell is accordingly estimated to be $p = 0.998$. For the same calculation for the SE shell, we derive

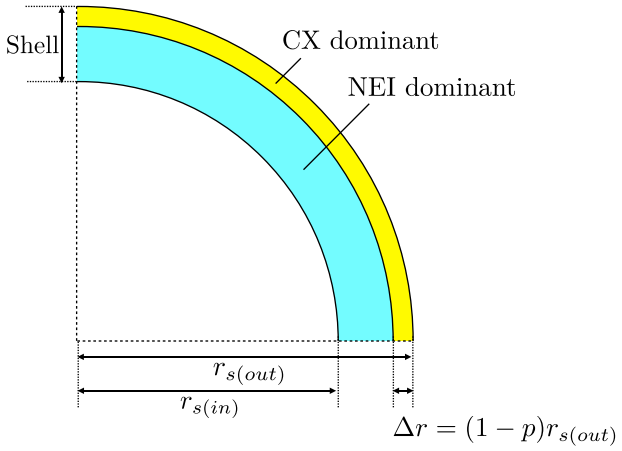

Figure 8. Geometry of shells we assumed for the calculation described in the text. The cyan and yellow represent NEI- and CX-dominant regions, respectively.

$V_{CX}/V_{NEI} = 9.2 \times 10^{-3}$ and $p = 0.997$, where we assume $r_{s(\mathrm{out})} = 4$ pc, $r_{s(\mathrm{in})} = 2$ pc, and $V_{NEI} \sim 2 \times 10^{57}$ cm^3.

While Lallement (2004) estimated that ∼1% of the shock radius is CX dominant based on the observation of the entire region of DEM L71, our estimate from partial shells of the nearby SNR G296.1−0.5 provides a more accurate measurement of p than before. The obtained values are $p = 0.998$ and $p = 0.997$ for the NW and SE, respectively, which means 0.2%–0.3 of the shock radius is CX dominant. Our result clearly indicates that CX is occurring at the outermost edge of the shock front. This is consistent with a general picture expected in SNRs. Similar anomalous f/r ratios have also been reported recently in other SNRs. In these examples, the RS effect would be more preferable than CX if p is much smaller (or V_{CX}/V_{NEI} is much larger) than the above value (Suzuki et al. 2020).

4.3. Future Works

It is expected that different conditions such as the shock velocity, ambient density, and abundances lead to different line ratios of CX (Gu et al. 2016). In this context, G296.1−0.5 is the best case that enables us to study various locations within the same object. As indicated in Figure 6, another region where we predict to detect CX is the southernmost shell interacting with Cloud 3. Since this shell is farthest from the SNR center, a higher forward shock velocity is expected, which may result in

京都大学 KYOTO UNIVERSITY
A Self-archived copy in
Kyoto University Research Information Repository
https://repository.kulib.kyoto-u.ac.jp
京都大学学術情報リポジトリ KURENAI 紅 Kyoto University Research Information Repository

a different line ratio from those in the other shells. In contrast, the northernmost edge of the NW shell can be interpreted to be unlikely that CX is occurring, because this region has little correlation with the ^{12}CO emission. These regions have a similar spatial width to the NW and SE shells and therefore future observations with the RGS will unveil the presence of CX almost entirely in G296.1−0.5.

If we assume our result can be applied to other nearby SNRs, it is possible to identify regions where CX is dominantly occurring. As pointed out in several studies (Katsuda et al. 2012; Roberts & Wang 2015; Uchida et al. 2019), the Cygnus Loop is one of the plausible candidates for detecting CX. Given that the Cygnus Loop has a spherical shell with an apparent diameter of 3°, we expect that a pure CX emission can be detected in a thickness of ∼15″ from the shock front. If this is the case, XRISM Resolve (Tashiro et al. 2018), which has a pixel size of ∼30″, is likely to detect a CX-dominant spectrum in the outermost edge of the remnant. Athena X-ray Integral Field Unit (Pajot et al. 2018) and Lynx X-ray Microcalorimeter (Gaskin et al. 2019) will provide us with a larger sample of SNRs, in which we can extract only CX X-ray emission.

5. Conclusion

We performed high-resolution spectral analysis of two shell regions (NW and SE) of G296.1−0.5 with the RGS on board XMM-Newton and discovered that the f/r ratio s of O VII Heα are significantly higher in both the shells than those expected from a normal NEI model. This is the first time that such an anomalous O VII Heα line is detected from multiple locations in a single remnant, although similar results have been obtained from observations of other SNRs (e.g., Uchida et al. 2019). The spectra of the NW and SE shells are well represented by incorporating a CX model with the previously reported NEI model. We also revealed that G296.1−0.5 is interacting with molecular clouds in several locations including the NW and SE, which is based on our ^{12}CO($J = 1$–0) and H I observation around the remnant. These results strongly support a picture that CX is occurring in the region where high f/r ratios are detected. These molecular clouds have velocities of $V_{\rm LSR} = -30$ km s^{-1} to -15 km s^{-1}, from which we estimated the distance to G296.1−0.5 to be 2.1 kpc. Assuming a spherical geometry, we calculated the contribution of the CX emission in the shells and concluded that CX is dominant in a region with a thickness of 0.2%–0.3% of the shock radius (collision parameter $p \sim 0.997$–0.998). This is consistent with a previous theoretical calculation by Lallement (2004). The obtained value of p will be useful for future observations with high-resolution spectroscopy such as XRISM and Athena to quantitatively evaluate a CX-dominant region in nearby SNRs.

The NANTEN project is based on a mutual agreement between Nagoya University and the Carnegie Institution of Washington (CIW). We greatly appreciate the hospitality of all the staff members of the Las Campanas Observatory of CIW. We are thankful to many Japanese public donors and companies who contributed to the realization of the project. This work is supported by JSPS KAKENHI Scientific Research grant Nos. JP19K03915 (H.U.), JP22H01265 (H.U.), JP19H01936 (T.T.), JP20KK0309 (H.S.), JP21H01136 (H. S.), and JP21H04493 (T.G.T and T.T.).

ORCID iDs

Yukiko Tanaka https://orcid.org/0000-0003-1857-7425
Hiroyuki Uchida https://orcid.org/0000-0003-1518-2188
Takaaki Tanaka https://orcid.org/0000-0002-4383-0368
Yuki Amano https://orcid.org/0000-0003-4520-9505
Yosuke Koshiba https://orcid.org/0000-0002-3119-2928
Takeshi Go Tsuru https://orcid.org/0000-0002-5504-4903
Hidetoshi Sano https://orcid.org/0000-0003-2062-5692
Yasuo Fukui https://orcid.org/0000-0002-8966-9856

References

Amano, Y., Uchida, H., Tanaka, T., Gu, L., & Tsuru, T. G. 2020, ApJ, 897, 12
Bolatto, A. D., Wolfire, M., & Leroy, A. K. 2013, ARA&A, 51, 207
Brand, J., & Blitz, L. 1993, A&A, 275, 67
Broersen, S., Vink, J., Kaastra, J., & Raymond, J. 2011, A&A, 535, A11
Castro, D., Slane, P. O., Gaensler, B. M., Hughes, J. P., & Patnaude, D. J. 2011, ApJ, 734, 86
den Herder, J. W., Brinkman, A. C., Kahn, S. M., et al. 2001, A&A, 365, L7
Dickey, J. M., & Lockman, F. J. 1990, ARA&A, 28, 215
Gaskin, J., Swartz, D., Vikhlinin, A., et al. 2019, JATIS, 5, 021001
Gaustad, J. E., McCullough, P. R., Rosing, W., & Van Buren, D. 2001, PASP, 113, 1326
Gu, L., Kaastra, J., & Raassen, A. J. J. 2016, A&A, 588, A52
Hwang, U., & Markert, T. H. 1994, ApJ, 431, 819
Kaastra, J. S., & Mewe, R. 1995, A&A, 302, L13
Kaastra, J. S., Mewe, R., & Nieuwenhuijzen, H. 1996, in 11th Coll. on UV and X-ray Spectroscopy of Astrophysical and Laboratory Plasmas, 411
Katsuda, S., Tsunemi, H., Mori, K., et al. 2011, ApJ, 730, 24
Katsuda, S., Tsunemi, H., Mori, K., et al. 2012, ApJ, 756, 49
Kerr, F. J., & Lynden-Bell, D. 1986, MNRAS, 221, 1023
Koo, B.-C., Reach, W. T., Heiles, C., Fesen, R. A., & Shull, J. M. 1990, ApJ, 364, 178
Koshiba, Y., Uchida, H., Tanaka, T., et al. 2022, PASJ, in press
Lallement, R. 2004, A&A, 422, 391
Lodders, K., Palme, H., & Gail, H. P. 2009, LanB, 4B, 712
Longmore, A. J., Clark, D. H., & Murdin, P. 1977, MNRAS, 181, 541
Markert, T. H., Lamb, R. C., Hartman, R. C., Thompson, D. J., & Bignami, G. F. 1981, ApJL, 248, L17
McClure-Griffiths, N. M., Dickey, J. M., Gaensler, B. M., et al. 2005, ApJS, 158, 178
Mizuno, A., & Fukui, Y. 2004, in ASP Conf. Ser. 317, Milky Way Surveys: The Structure and Evolution of our Galaxy, ed. D. Clemens, R. Shah, & T. Brainerd (San Francisco, CA: ASP), 59
Morrison, R., & McCammon, D. 1983, ApJ, 270, 119
Pajot, F., Barret, D., Lam-Trong, T., et al. 2018, JLTP, 193, 901
Roberts, S. R., & Wang, Q. D. 2015, MNRAS, 449, 1340
Sano, H., & Fukui, Y. 2021, Ap&SS, 366, 58
Seta, M., Hasegawa, T., Dame, T. M., et al. 1998, ApJ, 505, 286
Snowden, S. L., Collier, M. R., & Kuntz, K. D. 2004, ApJ, 610, 1182
Suzuki, H., Yamaguchi, H., Ishida, M., et al. 2020, ApJ, 900, 39
Tamura, T., Kaastra, J. S., den Herder, J. W. A., Bleeker, J. A. M., & Peterson, J. R. 2004, A&A, 420, 135
Tashiro, M., Maejima, H., Toda, K., et al. 2018, Proc. SPIE, 10699, 1069922
Turner, M. J. L., Abbey, A., Arnaud, M., et al. 2001, A&A, 365, L27
Uchida, H., Katsuda, S., Tsunemi, H., et al. 2019, ApJ, 871, 234
van der Heyden, K. J., Bleeker, J. A. M., Kaastra, J. S., & Vink, J. 2003, A&A, 406, 141
Wachter, K., Leach, R., & Kellogg, E. 1979, ApJ, 230, 274
Whiteoak, J. B. Z., & Green, A. J. 1996, A&AS, 118, 329